Manuscript Received: 26 Nov. 2025, Revised: 13 Feb. 2026, Accepted: 15 Feb. 2026
https://doi.org/10.36481/diujst.v21i1.daq3ez91

First-Principles Study of Structural and Electrical Properties of $SrFe_{12}O_{19}$ Nanoparticles

Md. Roni.Islam*

Department of Computer Science and Engineering (CSE), Daffodil International Univeristy (DIU), Savar-1340, Ashulia, Dhaka,Bangladesh.

***Corresponding author: roniislam.cse@diu.edu.bd**

***Abstract*: Sol–gel synthesis was used to prepare M-type strontium hexaferrite ($SrFe_{12}O_{19}$) nanoparticles, which were thoroughly analyzed through both first-principles calculations and experimental characterization techniques. The phase formation and structural development were investigated using X-ray powder diffraction along with Rietveld refinement, confirming the formation of a highly crystalline single-phase hexagonal magnetoplumbite structure with space group $P6_3/mmc$. No impurity phases were detected, while systematic peak broadening was observed without any noticeable peak shifting. The lattice parameters *a* and *c* were found to of 5.776 Å and 22.054Å, respectively. Dielectric constant and AC electrical resistivity exhibited enhanced values, and dielectric measurements revealed relaxation behavior at higher frequencies. Density functional theory calculations within the GGA-PBE framework indicate a semiconducting nature with an indirect band gap of approximately 1.81 eV, dominated by Fe-3d and O-2p electronic states. Optical analysis demonstrates strong ultraviolet absorption, low reflectance in the visible region, and a pronounced dielectric response, while elastic property evaluation confirms direction-dependent mechanical behavior due to elastic anisotropy. These results suggest that $SrFe_{12}O_{19}$ nanoparticles are promising candidates for advanced magnetic devices, optoelectronic applications, and microwave miniaturization technologies.**

Index Terms: Structural parameters, Electrical parameters, Hexagonal ferrite, Nanoparticles, First principle approach.

1. INTRODUCTION

Due to their unique physical and chemical characteristics, hexagonal ferrites have attracted a lot of attention ever since their discovery [1]. M-type strontium (Sr) hexaferrites ($M{\cdot}6Fe_2O_3$, where M = Sr) are widely utilized in various applications, including information technology (IT), microwave-absorbing paints, anti-electromagnetic interference systems, telecommunications, channel filters, magnetic recording, magneto-optic and gyromagnetic devices, as well as multilayer chip devices [2].Due to their high resistivity, chemical stability, high Hc, high Ms, and affordable synthesis, M-type hexaferrites are interest- ing[3]. There are six different types of iron oxides: M-type ($PFe_{12}O_{19}$, X-type ($P_2Q_2Fe_{20}O_{46}$), Y-type ($P_2Q_2Fe_{12}O_{22}$), W-type ($PQ_2Fe_{16}O_{27}$) and U-type ($P_4Q_2Fe_{36}O_{60}$) phases were P can be Ca, Sr, Pb, Ba, and Q can be bivalent cations of transition metals like Ni, Co, or Zn [4]. M-type hexaferrites belong to the space group P63/mm.c. Three octahedral locations (2a, 12k, and 4f2), one tetrahedral site (4f1), and one bipyramidal site (2b) contain the Fe3+ ions. Three locations (2a, 2b, and 12k) contain spin-up ions, and two locations (4f1 and 4f2) have spin-down ions [5]. The intrinsic characteristics of M- type hexaferrites have been shown to be strongly influenced by both the cationic substitutes and synthesis techniques [6].

2. LITERATURE REVIEW

When lanthanide ions [7] or transitional metal ions are added to M-type hexaferrites, the structural and dielectric characteristics change significantly [8] are substituted. Litsardakis et al. reported that, Gd-substituted chemical co-precipitation approach was used to synthesize barium hexaferrites ($(Ba_{1-x}Gd_x)O{\cdot}5.25Fe_2O_3$ (x = 0–0.30), and the saturation magnetic strength at 1.8 T varies significantly with x, but a significant improvement is found for all replaced samples [9].Xie et al. reported that, Co-precipitation high-temperature sintering was used to create the cobalt-substituted strontium hexaferrite $SrCo_xFe_{12-x}O_{19}$ (x = 0-0.3), with $SrCo_xFe_{12-x}O_{19}$ (x = 0.3) having a higher saturation magnetization than $SrCo_xFe_{12-x}O_{19}$ (x = 0.2). Co-substituting lanthanide and transition metal ions can also dramatically alter the magnetic properties of M-type hexaferrites [10]. According to Litsardakiset al. shown that, the $Ba_{1-x}Gd_xFe_{12-x}Co_xO_{19}$ (x = 0.0–0.4) Gd-Co-substituted hexaferrites were synthesized using the traditional ceramics technique, and specimens with x = 0.1–0.2

have coercive property values that are as much as 15 percent greater than those of $BaFe_{12}O_{19}$ while having lower saturation magnetic characteristics and remanence values.

The M-type hexaferrites can be made synthetically in a variety of ways, such as by the chemical co-precipitation approach [11]. Treatment with heat occurred after the Zr-Mn doped M-type strontium hexaferrites had been generated via sol-gel auto-combustion. Alamolhoda et al. found that coercivity dropped from 5593.60 to 3282.46 Oe and the greatest magnetic field dropped from 62.60 to 46.15 emug-1 as the Zr-Mn composition rose.The Zr-Mn doped M-type strontium hexaferrites were created by sol-gel auto-combustion and subsequently heated. Alamolhoda et al. found that coercivity dropped from 5593.60 to 3282.46 Oe and the greatest magnetic field reduced from 62.60 to 46.15 emug^{-1} as the Zr-Mn composition rose [12]. Numerous studies on M-type hexaferrites with cou- pled substitution have been conducted, including those on Zr- Mn[13], La-Zn[14], Zr-Mg[15], Mn-Zn[16], La-Co[17], Zn-Ti[18], La-Cu [19], and Co-Zr[20].The M-type hexaferrites can be produced synthetically in a variety of ways, including sol-gel [14], sol-gel auto-combustion[21], hydrothermal[22], chemical co-precipitation[13], Pechini method [23],standard ceramic method [24], reverse micelle method [25], citrate pre- cursor[26], and molten flux methods[27].

Recently, Zainullina *et al.* investigated using ab initio linear muffin-tin orbital calculations within the tight-binding approximation (LMTO–TB) and semi-empirical extended Huckel theory (EHT), the electronic structure, chemical bonding, and ion conductivity of lead hexaferrite PbFe12O19 were investigated. However, the magnetic structure of $PbFe_{12}O_{19}$ was not explored in their study. Co occupancy at different Fe sublattices was studied by Nakamura et al., but the theoretical treatment lacked a thorough and resolved DFT investigation across all main replacement sites, especially when formation energy differences are small. Although the beneficial effects of Co doping at the 4f1 site on magnetic performance were highlighted in our earlier study, the microscopic sources**,** including the bond population trends and electronic redistribution, were not thoroughly addressed [28]. In this work, we synthesized M-type strontium hexaferrites, or $SrFe_{12}O_{19}$ using the sol-gel method. X-ray diffraction and electrical character analysis were used for studying the effect of the structural and dielectric characteristics of M-type strontium hexaferrites.

3. METHODOLOGY

M-type SrFe12O19 specimens were created by the sol–gel technique. The precursor materials included ferric nitrate [Fe(NO3)3·9H2O, 98%, Merck] and strontium nitrate [Sr(NO3)2, 98%, LOBA Chemical] in the proper stoichiometric quantities. Citric acid [C6H8O7·H2O, 99%, Merck] is used to make the sol and a small amount of HCl were dissolved in filtered distilled water and used as chelating agents. The resulting solution was stirred continuously until a homogeneous precursor solution was obtained.

The methodical sol-gel synthesis process used to create strontium hexaferrite (Sr-hexaferrite) nano-powders is shown in Figure 1. To guarantee high purity and uniform ionic distribution, the necessary metal ions (Sr^{2+}, Fe^{3+}, Gd^{3+}, and Cu^{2+}) are first dissolved individually in distilled water. After that, a precursor solution is created by combining these aqueous solutions and stirring it constantly for a few hours. Extended stirring accelerates the chelation and hydrolysis reactions required for sol formation and encourages homogeneous mixing at the molecular level.

The homogeneous solution progressively changes into a sol as the reaction carries on, and this sol then goes through polycondensation to create a gel. The gel is a three-dimensional network of evenly spaced metal ions. After that, the gel is heated to 120 °C for a whole day, which eliminates extra solvent and organic residues and leaves behind a dry precursor powder. The residual organic components are broken down, crystallinity is improved, and phase formation is encouraged by calcining this powder for four hours at 750 °C. Ultimately, the intended Sr-hexaferrite nano-powder is produced by calcination. Compared to traditional solid- state synthesis techniques, this sol-gel process offers superior control over particle size, chemical homogeneity, and phase purity, making it appropriate for the production of doped hexaferrite nanomaterials.

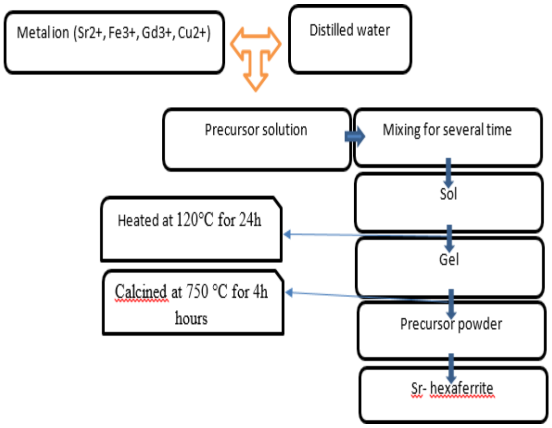

Fig. 1. Diagram illustrating the sol-gel process flow chart for preparing samples of Sr- hexaferrite nano-powders.

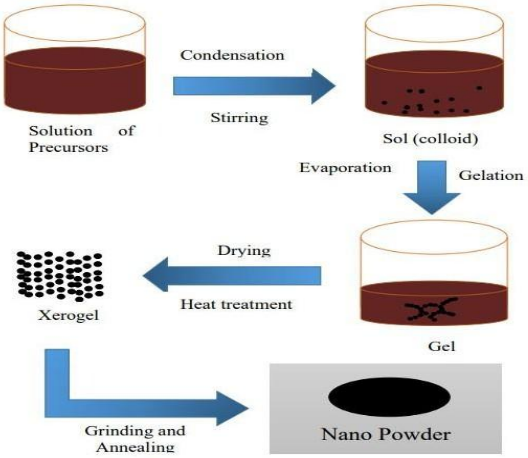

Fig. 2. Diagram illustrating the experimental setup for preparing samples of Sr-hexaferrite nano-powders.

Fig. 2 Diagrammatic representation of the sol-gel process showing the transformation from precursor solution to sol via condensation and stirring. Gelation occurs through evaporation, followed by drying and heat treatment to form a xerogel. Finally, grinding and annealing convert the xerogel into nanocrystalline powder.

4. RESULTS & DISCUSSION

A. XRD Refinement Analysis

X-ray diffraction is a method for figuring out the results of the sample crystal form or substance. To ascertain the structure of atoms in bigger crystals, such as macromolecules and inorganic compounds, it is employed. Phase purity, crystallinity, and sample composition can all be ascertained for smaller crystals. The measurement of the wavelength of X-ray beams is comparable to the distance between atoms in the sample, which is why they are used. Beams of comparable wavelengths combine to form a new beam with a greater amplitude, a phenomenon known as constructive interference. Atomic plane differences can be identified with this diffraction angle. Figure 3 illustrates the X-ray diffraction (XRD) spectrum of the generated $SrFe_{12}O_{19}$ nanoparticles.

The pure hexagonal magnetoplumbite structure with a space group of $P6_3/mmc$ can be identified by the sample's XRD patterns (JCPDS card No. 84-1531) [29].

For every diffraction pattern obtained, powder XRD data were improved using a Philips X- Pert Pro X-Ray Diffractometer 2theta value 10 to 80 degrees. The majority of the detected peaks correspond to the resultant product of $SrFe_{12}O_{19}$, with a very minor Fe_2O_3 (JCPDF: 33-0664) residual phase. The observed high intensity and sharp, well-defined peaks indicate a high crystalline quality. The resultant product exhibits consistency between all of its diffraction peaks and those of the single phase [30]. The diffraction planes (1 1 0), (1 0 7), (1 1 4),(2 0 1), (2 0 3), (2 0 5), (2 0 6), (3 0 0), (2 1 7),(2 0 11),, (2 2 0), (2 0 13), (2 0 15) and (3 1 7) were associated with the peaks that were visible in the XRD pattern. These planes are essential for the M-type hexaferrite diffraction peaks.

There are some Bragg diffraction planes (0 1 2), (1 0 4), (1 1 3), (0 2 4), (2 1 1), (0 1 8) and (2 1 4) of Fe_3O_4 were associated in the XRD. $SrFe_{12}O_{19}$ has exist lattice parameter 'a' and 'c' are values 5.872Angstrom and 22.065Angstrom and crystallite size was calculated to be 30.886 Angstrom. It has x-ray density, bulk density and porosity are calculated as 5.35g/cm^3, 2.32g/cm^3 and 7.2 percent. It has also c/a ratio value 3.758Angstrom which is identified the sample crystal synthesis formatted.

B. Electric Structure:

Strontium hexaferrite, or $SrFe_{12}O_{19}$, is a ferrimagnetic substance whose intricate crystal structure greatly affects its electrical characteristics. This is how its electrical structure is explained:

1. Crystal Organization/ Structure:

Strontium hexaferrite or ($SrFe_{12}O_{19}$) belongs to the $P6_3/mmc$ space group and has a hexagonal crystal shape. There are 64 ions in the unit cell: 2 Sr^{2+}, 24 Fe^{3+} and 38 O^{2-}ions**.** Figure 4 shows that Fe^{3+} ions occupy five distinct crystallographic sites: one tetrahedral site ($4f_1$), one trigonal bipyramidal site (2b), and three octahedral sites (12k, $4f_2$, and 2a).

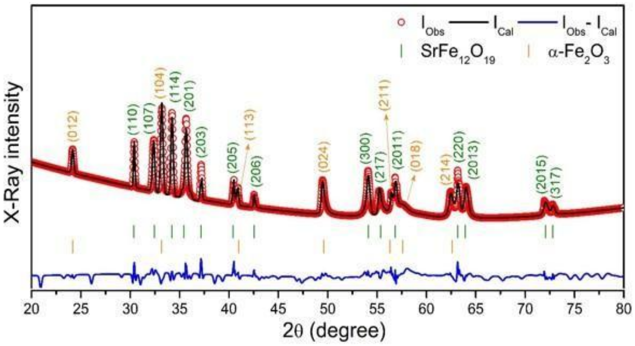

Fig. 3. The XRD patterns of $SrFe_{12}O_{19}$ nanoparticles

TABLE I

Rietveld-refined structural parameters and phase fractions (wt%) derived from XRD analysis of the $SrFe_{12}O_{19}$ sample, including χ^2 (goodness of fit), Rp (unweighted pattern residuals), and Rwp (weighted pattern residuals).

Crystal Structure	*Phase percent-ages (wt%)*	*Lattice Parameters (Angstrom)*	*Unit cell Volume*	*R Factor (per-cent)*	
$SrFe_{12}O_{19}$ $P6_3/mmc$ (Hexagonal)	78.6 ± 1.0	a = b = 5.8761 (3) c = 23.0239 (3)	688.5 (1)	Rp = 8.7 Rwp = 7.2	2.5
Alpha Fe_2O_3 R-3c (Rhom-bohedral)	21.4 ± 0.3	a = b = 5.0316 (2) c = 13.7285 (2)	301.1 (1)	Rp = 6.8 Rwp = 5.9	2.35

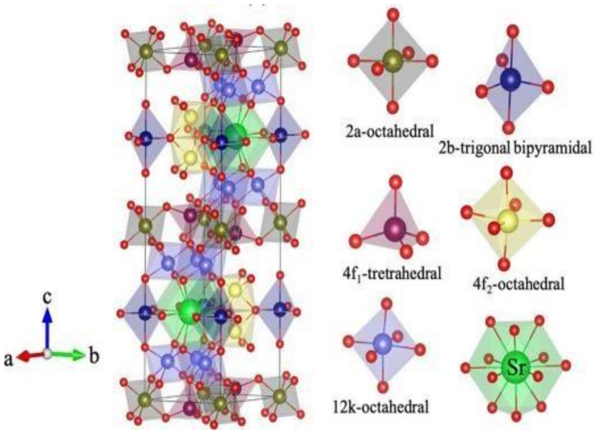

Fig. 4. The unit cell of strontium hexaferrite ($SrFe_{12}O_{19}$) nanoparticles

2. Electronic Configuration:

The main factor influencing the electrical structure of $SrFe_{12}O_{19}$ is the presence of Fe^{3+} ions. The magnetic characteristics of each Fe^{3+} ion are derived from their electronic configuration, which is [Ar] $3d^{5+}$, with five unpaired electrons in the d-orbitals.**)**

C. Density Functional Theory (DFT)

First-principles calculations for M-type hexaferrite $SrFe_{12}O_{19}$ were conducted using density functional theory (DFT). The exchange–correlation energy was described using the Perdew–Burke–Ernzerhof (PBE) functional within the generalized gradient approximation (GGA). The interaction between core and valence electrons was modeled using the projector augmented wave (PAW) method. A plane-wave energy cutoff of 520 eV was applied to ensure accurate convergence. Brillouin zone sampling was performed using a 5 × 5 × 1 Monkhorst–Pack k-point grid. Structural optimization was continued until the total energy converged to 10^{-6} eV and the residual forces on each atom were reduced below 0.01 eV/Å.

In this study, we systematically explored the influence of La^{3+} and Co^{2+} doping on the magnetic and electronic properties of $SrFe_{12}O_{19}$ using density functional theory (DFT) calculations supported by experimental validation. Five representative compositions were analyzed, including pristine SFO, La-doped SFO, and La–Co co-doped variants with Co occupying the $4f_1$, 12k, and 2a crystallographic sites, respectively [31]. The electrical and magnetic properties of $A_xSr_1{-}_xFe_{12}{-}_xM_xO_{19}$ hexaferrites (A = alkali elements, M = transition metals) were also investigated by Ahn et al. through combined experimental and theoretical approaches. Their study showed that La^{3+} is an effective co-dopant for $SrFe_{12}{-}_xCo_xO_{19}$, compensating for the charge imbalance caused by Co^{2+} substitution. Additionally, alkali elements such as Na and K were found to be suitable for (V/Nb/Ta)-doped $SrFe_{12}O_{19}$, with Na/K–V co-doping significantly enhancing intrinsic coercivity [32].

The calculated electronic structure of $SrFe_{12}O_{19}$(strontium hexaferrite) reveals detailed insights into its electronic and magnetic properties, derived primarily through first-principles methods like density functional theory (DFT). Below, we outline the key features of its electronic structure: (a) Band Gap, (b)Density of States (DOS), (c) Valence Band (d) Conduction Band.

(a) **Band structure**:

A two-dimensional representation of the energies of the crystal orbitals in a crystalline material is called the band structure [33]. In essence, it is a depiction of a solid material's permitted electronic energy levels. It is possible to determine whether a material is metallic, semi-metallic, or insulating by looking at its band structure graph. The character and energy of the prominent bands close to the Fermi level can be used to study a variety of material features. A material's optical qualities, electrical conductivity, electronic heat capacity, magnetic properties, Hall voltage, and additional data are all exposed by the band structure curve. A band structure's number of bands is equal to the number of atomic orbitals in a unit cell. The band arrangements of the hexagonal phases employing GGA functionals are shown in Fig. 5. The Fermi energy is zero in this instance.

The high symmetry sites of the Brillouin zone and the energy band structures of SrFe12O19 as a function of energy (E-EF) were computed at zero temperature and pressure. The Fermi level (E_F) is shown as the horizontal broken line. The hexagonal phases have band gap values of 1.81 eV each. The image presents an electronic band structure diagram. In essence, it illustrates how the energy levels of electrons in a crystal ($SrFe_{12}O_{19}$ in this case) vary with their momentum or wave vector (represented along the horizontal axis, labeled "k Point").Energy Axis (Vertical): The y-axis represents the energy of the electrons in electron volts (eV).k- Point Axis (Horizontal): The x-axis represents different points in the Brillouin zone, which is the fundamental region of the crystal's momentum space. High-symmetry points in the Brillouin zone are labeled (G, A, H, K, G, M, L, H). Bands: the electronic band structure is illustrated by the blue lines shown in the diagram, where each band represents the allowed energy levels that electrons can occupy. The band gap (Eg) corresponds to the energy difference between the top of the highest occupied band (valence band) and the bottom of the lowest unoccupied band (conduction band). In the figure, the band gap is indicated as Eg = 1.81 eV. The band structure of $SrFe_{12}O_{19}$ suggests that the material behaves as an insulator.

The presence of a bandgap (Eg = 1.81 eV) indicates that there's an energy barrier that electrons must overcome to move from the valence band to the conduction band. In insulators, this energy barrier is relatively large, preventing the flow of electricity under normal conditions. Our calculated bandgap values using both GGA-PBE and LDA functionals are greater than the experimental ones [34] due to the well-known drawback of DFT, but they accord well with the previously published values [35, 36]. This is because DFT is often unable to predict semiconductors and insulators' excited or unoccupied states with sufficient accuracy [37]. $SrFe_{12}O_{19}$ with a band gap of ~1.81 eV is suitable for electronic and sensor applications due to its visible-light activity and ferrimagnetic nature. It can be used in gas sensors, photodetectors, and magneto-electronic or spintronic devices, offering good stability, low cost, and multifunctional performance for next-generation electronics.

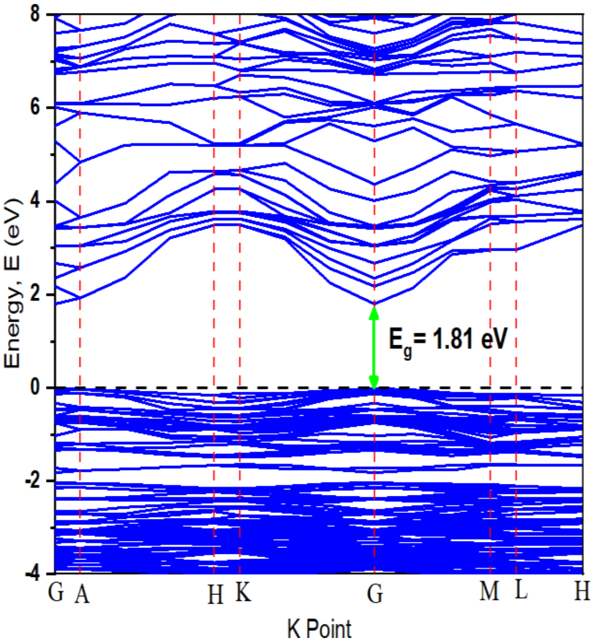

Fig. 5. The band structure of strontium hexaferrite ($SrFe_{12}O_{19}$) nanoparticles at first principle study.

D. Density of state (DOS)

Electronic energy density of states (DOS) in condensed physics is the number of electronic states available at each energy level per unit energy interval. In most crystalline solids, the structure of the DOS impacts the electrical and optical properties, such as conductivity, magnetic order, bonding versus antibonding states, optoelectronic characteristics, and many more [36]. Figure 5 presents the total and partial density of states (TDOS and PDOS) for five hexagonal $SrFe_{12}O_{19}$ nanoparticles. The Fermi level (EF), which separates the bonding and antibonding states, is indicated by a vertical dashed line in the figure. The PDOS of Sr, Fe, and O atoms is analyzed to better understand their contributions to the TDOS and the nature of chemical bonding. There are two electric states present for oxygen (O) such as O-2s and O-2p states. Again, the electric states for iron

(Fe) and strontium (Sr) have three electric states such as Fe-3s, Fe-3p, Fe-3d and Sr-5s, Sr-4p, Sr-3d respectively.

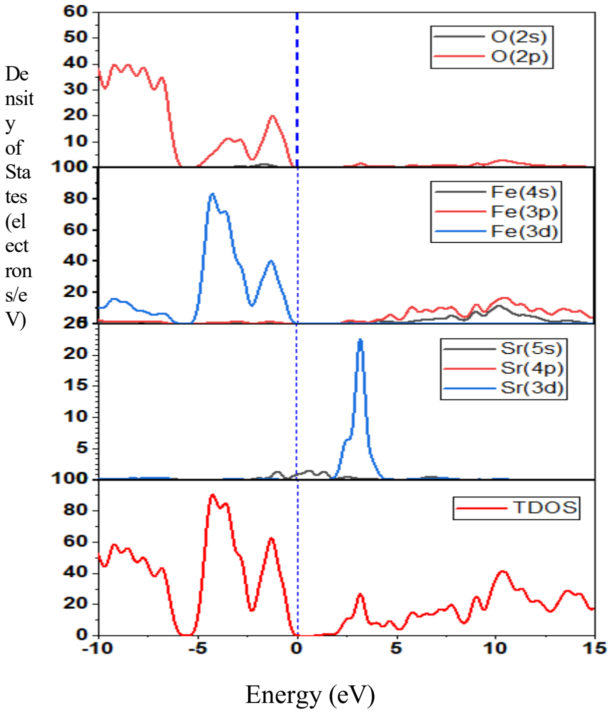

Fig. 6. Total DOS and partial DOS hexagonal phases of $SrFe_{12}O_{19}$

E. Theoretical Optical Properties

Photons interact with materials, defining their optical properties. This interaction is crucial for determining applications in absorbers, reflectors, optical coatings, and optoelectronics. Energy band structure, impurity levels, excitons, defects, lattice vibrations, and magnetic excitations are all studied by energy-dependent optical properties.

Dielectric properties:

One important component of optical spectroscopy, the dielectric function $\varepsilon(\omega)$, can be deter- mined by employing electronic band structure computations of a solid. The electrical structure becomes clearer when optical functions are studied. In terms of energy, the complex dielectric function can be used to predict a material's linear response to an external electromagnetic field. $SrFe_{12}O_{19}$ optical characteristics were computed using the frequency-dependent complex dielectric function [38]. The Kramers- Kronig relation can be used to derive $\varepsilon_1(\omega)$, which is related to the electronic transition, from $\varepsilon_2(\omega)$. The optical characteristics of $SrFe_{12}O_{19}$ up to 45 eV have been investigated in this work, along with several polarization orientations ([100], [010], and [001]) for the incident electric field. The imaginary component of the dielectric functions for the hexagonal phases of $SrFe_{12}O_{19}$ is shown in Fig. 7. The dielectric function's imaginary component is shown to have notable peaks at 5.31, 5.16, and 5.08 eV for hexagonal phases with polarization directions of [001], [100], and [100], respectively, supporting the phases' optical anisotropy (Fig. 7). The material's dielectric function reflects all electromagnetic radiation in the energy range, with lower energies primarily due to electronic transitions and higher energies due to plasma resonances.

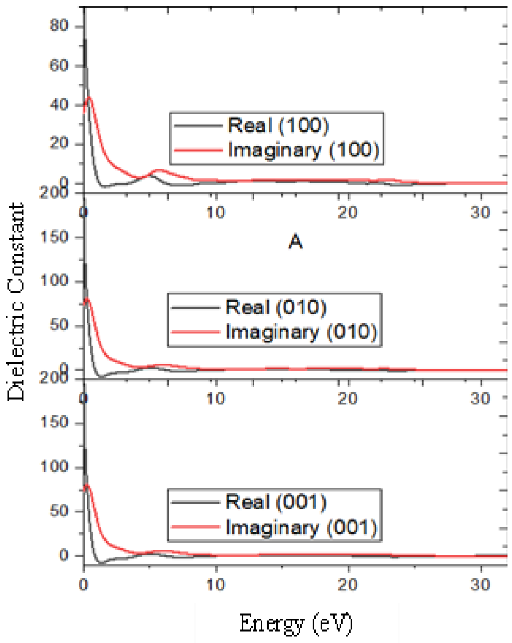

Fig. 7. Dielectric constant vs energy hexagonal phases of $SrFe_{12}O_{19}$

1. *Conductivity*:

One essential optical metric for comprehending electromagnetic responses is optical conductivity. It indicates electrical conductivity when there is an alternating electric field. The photoconductivity of a material is defined as the conductivity of free-charge carriers within a given range of photon energy [40]. Fig. 8 displays the calculated frequency- dependent optical conductivity $\sigma(\omega)$ of $SrFe_{12}O_{19}$.

2. *Absorption*:

The optical absorption coefficient measures light permeability and optimal solar energy con- version efficiency. Absorption spectra help identify electronic transitions in energy bands, aiding in the utilization of materials in solar cells. Fig. 9 displays the absorption coefficient spectra of $SrFe_{12}O_{19}$. The fact that the spectra do not begin at zero energy levels and rapidly increase with increasing photon energy confirms its semiconducting nature. Since the ultraviolet (UV) region of all $SrFe_{12}O_{19}$ nanoparticles exhibits maximal absorption due to their wide bandgap values, this material will be an excellent absorber when exposed to UV radiation. According to the imaginary component of the dielectric constant, the various absorption peaks result from the different inter-band optical transitions.

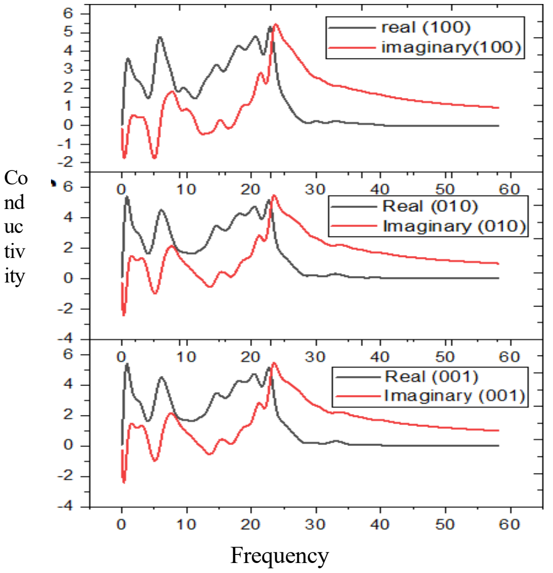

Fig. 8. Conductivity vs frequency for real & imaginary constant hexagonal phases of $SrFe_{12}O_{19}$

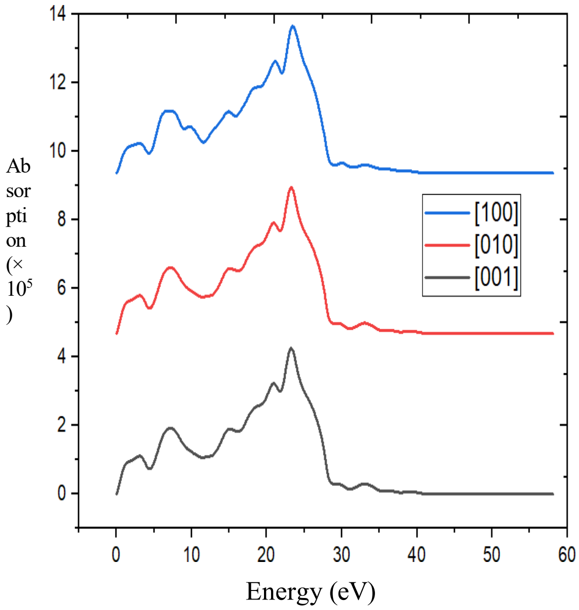

Fig. 9. Absorption vs energy for real & imaginary constant hexagonal phases of $SrFe_{12}O_{19}$.

3. *Loss function:*

The amount of energy a fast electron loses when passing through a substance is shown by the energy loss spectrum. A substance's properties of absorption and reflection establish its loss function. Moreover, a material's peak in the loss function $L(\omega)$ corresponds to the trailing edges of its reflection spectrum. The energy loss function's response to the photon energy of $SrFe_{12}O_{19}$ is shown in Fig.10. The sharp decline of $R(\omega)$ coincides with the peak in $L(\omega)$ at 28.0 eV. The bulk plasma frequency, or ω_p, is defined as the peak and occurs when $\varepsilon_1(\omega) = 0$ and $\varepsilon_2(\omega) < 1$ [41]. For $SrFe_{12}O_{19}$, the plasma frequency appears at about 28 eV. $SrFe_{12}O_{19}$ exhibits insulator-like optical characteristics and becomes transparent to incident photons above the plasma resonance energies.

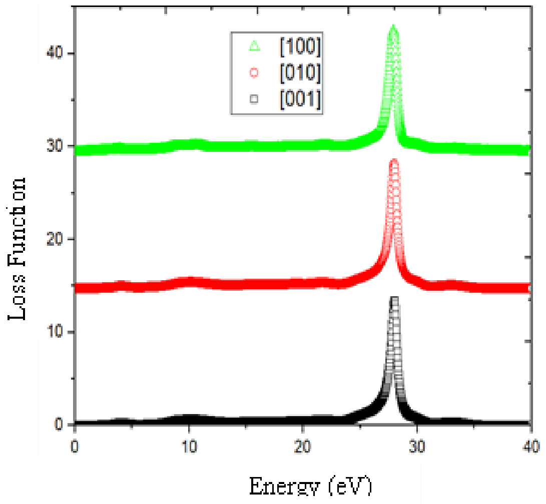

Fig. 10. Loss function vs energy curve for hexagonal phases of $SrFe_{12}O_{19}$

4. Reflectivity:

Reflectivity is a crucial optical parameter that allows one to calculate the ratio of light energy incidents on a material to the light energy reflected from it. The incoming photon energy-dependent reflectivity, or R(ω), of $SrFe_{12}O_{19}$ is shown in Fig. 11. In terms of reflectivity, a lower energy bandgap causes a greater ε1(0) value, which raises R(ω), and vice versa. All of the $SrFe_{12}O_{19}$ nanoparticles had extremely low reflectivity in the near UV-vis region, as seen in Fig. 11. Additionally, it is shown that the system becomes extremely transparent in the region where the reflectivity drops to zero, which occurs at about 13.3 eV. All the $SrFe_{12}O_{19}$ nanoparticles are clearly conducting oxides since the absorption coefficient is likewise low in this area. $SrFe_{12}O_{19}$ may therefore be a viable option for solar cell window materials. The greatest reflectance of the $SrFe_{12}O_{19}$ nanoparticles was reached at around 30 eV, which is in line with the system's plasma peaks.

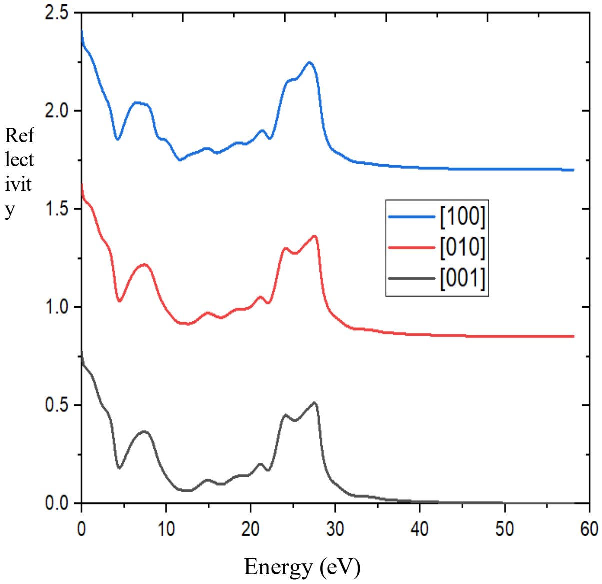

Fig. 11. Reflectivity vs energy curve for hexagonal phases of $SrFe_{12}O_{19}$

5. *Elastic Anisotropy:*

Anisotropy is a crucial parameter for determining if a material's structural properties are uniform in all directions. Understanding various anisotropy indices is essential since most known crystalline materials are anisotropic to varied degrees and because a material's direction-dependent mechanical behavior may be explained by its elastic anisotropy. The nature and degree of anisotropy in materials are closely related to several significant physical processes, including the development of plastic deformations in crystals, mechanical yield points, phase transformations, micro-scale cracking in solids, crack motion, and structural instability. For this reason, the study of the anisotropic elastic properties of materials is crucial. Three-dimensional (3D) and two-dimensional (2D) graphical perspectives are highly useful for better understanding elastic response and for visualizing the anisotropic mechanical behavior of materials.

The elastic anisotropy level in Young's modulus (E), linear compressibility (K), shear modulus (G), and Poisson's ratio (v) can be directly visualized on 2D projections and in a 3D spherical plot on the (xy), (yz), and (zx) planes using the open-source program ELATE [42]. The signs of an isotropic crystal are uniform circular 2D and spherical 3D graphical representations. The two and three-dimensional representations of the four elastic anisotropy levels—E, G, v, and K—are shown in Fig. 16. Figure 12 makes clear that each phase exhibits varied degrees of anisotropy. ELATE provides an additional numerical examination by showing the lowest and maximum values of each modulus as well as the directions of these extrema. This allows for the identification of the direction of particular significance for elastic properties, which do not necessarily have to be parallel to the crystallographic axes of the material. Anisotropy AX for each elastic modulus X is defined as follows:

$$A_X = X_{max} / X_{min} \ldots\ldots\ldots\ldots\ldots\ldots \textbf{(1)}$$

$$\text{if } sign\,(X_{max}) = sign\,(X_{min})$$

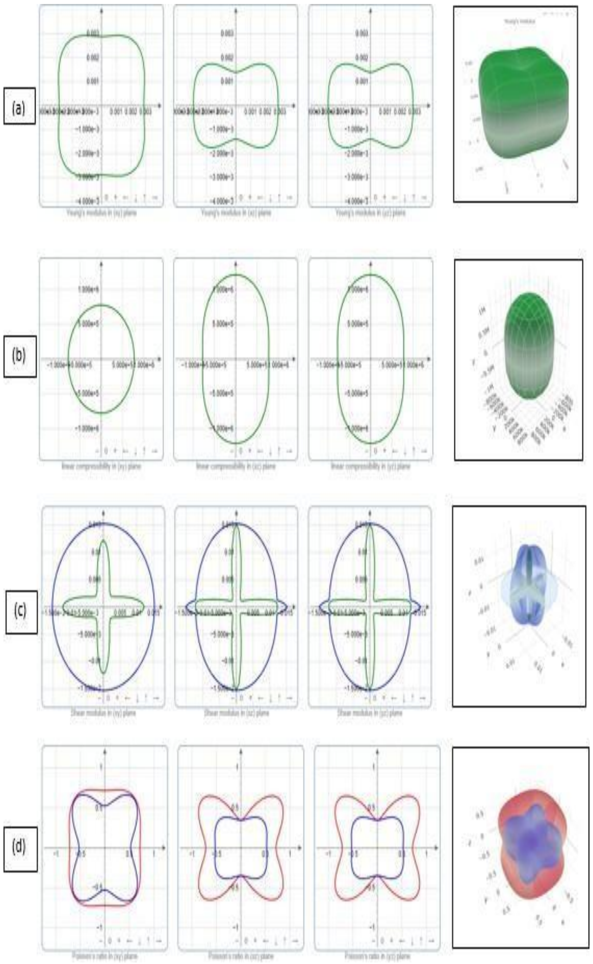

Fig. 12. Plots in two and three dimensions of the hexagonal phases of $SrFe_{12}O_{19}$ for (a) Young's modulus (b) linear compressibility (c) shear modulus and (d) Poisson's ratio.

6. CONCLUSION

The structural, electrical, photocatalytic, elastic, and optical characteristics of five polymorphs of $SrFe_{12}O_{19}$—cubic, rhombohedral, orthorhombic, tetragonal, and hexagonal—have all been examined in this work. These compounds' bonding characteristics and charge density distribution are also investigated. The calculations from the first principles have been performed using the CASTEP code, which is based on density functional theory. The synthetic materials' structural characteristics were ascertained by the use of XRD patterns. At zero pressure and temperature, a thorough optimization of the structural characteristics of the $SrFe_{12}O_{19}$ hexagonal has been carried out. Calculating the lattice parameters involves the use of GGA-PBE and LDA functionals. Among these, the outcomes produced by GGA-PBE exhibit strong concurrence with the existing experimental and theoretical findings. Because the GGA-PBE strategy yields somewhat more accurate results than LDA, that is the one we have chosen.

Based on the electronic band structure analysis and total density of states, all of the $SrFe_{12}O_{19}$ polymorphs seem to be semiconductors, with HSE06 functional levels that are fairly close to the reported band gap values of the nanomaterials. This analysis is the first that approaches the experimental band gap values of the nanomaterials quite closely. Furthermore, the examination of the fractional density of states (PDOS) and density of states (DOS) demonstrated the contributions of O and Fe atoms to the magnetic properties, confirming the dominance of Fe 3d states in $SrFe_{12}O_{19}$ magnetic features.

The success of DFT in modeling $SrFe_{12}O_{19}$ suggests its reliability for studying similar complex magnetic oxides. However, future studies may benefit from using more advanced hybrid functionals or GW corrections to further refine the electronic properties and explore temperature-dependent effects, which were not covered in this study. Overall, this research contributes to the growing body of knowledge on ferrite materials and supports the continued use of DFT in exploring their fundamental properties and potential applications in magnetic devices.

ACKNOWLEDGMENT

No one else has published this work, and no one else is considering it for publication. All participants are appreciative of the opportunity to offer their time and knowledge to this research.

REFERENCES

[1] M. A. Malana, R. B. Qureshi, M. N. Ashiq, and M. F. Ehsan, “Synthesis, structural, magnetic and dielectric characterizations of molybdenum-doped calcium strontium M-type hexaferrites,” *Ceram. Int.*, vol. 42, no. 2, pp. 2686–2692, Feb. 2016, doi: 10.1016/j.ceramint.2015.10.144.

[2] “A study on the microstructural and magnetic properties of the $Sr_{0.70-x}Ba_xLa_{0.30}Fe_{11.78}Cu_{0.22}O_{19}$ hexagonal ferrites,” *Int. J. Mod. Phys. B*. [Online]. Available:https://www.worldscientific.com/doi/abs/10.1142/S0217979214501409. Accessed: Mar. 18, 2024.

[3] Y.-M. Kang, “High saturation magnetization in La–Ce–Zn-doped M-type Sr-hexaferrites,” *Ceram. Int.*, vol. 41, no. 3, pp. 4354–4359, Apr. 2015, doi: 10.1016/j.ceramint.2014.11.125.

[4] “Magnetic and morphological characterization of $SrFe_{12}O_{19}$/PA12 composites: Hard-magnetic filament for magnetic field-assisted additive manufacturing (MFAAM),” *ProQuest*. [Online]. Accessed: Mar. 18, 2024.

[5] R. L. Palomino, A. M. Bolarín Miró, F. N. Tenorio, F. Sánchez de Jesús, C. A. Cortés Escobedo, and S. Ammar, “Sonochemical assisted synthesis of $SrFe_{12}O_{19}$ nanoparticles,” *Ultrason. Sonochem.*, vol. 29, pp. 470–475, Mar. 2016, doi: 10.1016/j.ultsonch.2015.10.023.

[6] R. C. Pullar, “Hexagonal ferrites: A review of the synthesis, properties and applications of hexaferrite ceramics,” *Prog. Mater. Sci.*, vol. 57, no. 7, pp. 1191–1334, Sep. 2012, doi: 10.1016/j.pmatsci.2012.04.001.

[7] C. Lei, S. Tang, and Y. Du, “Synthesis of aligned La^{3+}-substituted Sr-ferrites via molten salt-assisted sintering and their magnetic properties,” *Ceram. Int.*, vol. 42, no. 14, pp. 15511–15516, Nov. 2016, doi: 10.1016/j.ceramint.2016.06.204.

[8] Z. Mosleh, P. Kameli, A. Poorbaferani, M. Ranjbar, and H. Salamati, “Structural, magnetic and microwave absorption properties of Ce-doped barium hexaferrite,” *J. Magn. Magn. Mater.*, vol. 397, pp. 101–107, Jan. 2016, doi: 10.1016/j.jmmm.2015.08.078.

[9] G. Litsardakis, I. Manolakis, C. Serletis, and K. G. Efthimiadis, “High coercivity Gd-substituted Ba hexaferrites prepared by chemical coprecipitation,” *J. Appl. Phys.*, vol. 103, no. 7, p. 07E501, Apr. 2008, doi: 10.1063/1.2832857.

[10] T. Xie, L. Xu, and C. Liu, "Synthesis and properties of composite magnetic material $SrCo_xFe_{12-x}O_{19}$ (x = 0–0.3)," *Powder Technol.*, vol. 232, pp. 87–92, Dec. 2012, doi: 10.1016/j.powtec.2012.08.015.

[11] G. Litsardakis, I. Manolakis, and K. Efthimiadis, "Structural and magnetic properties of barium hexaferrites with Gd–Co substitution," *J. Alloys Compd.*, vol. 427, no. 1–2, pp. 194–198, Jan. 2007, doi: 10.1016/j.jallcom.2006.02.044.

[12] S. Alamolhoda, S. M. Mirkazemi, Z. Ghiami, and M. Niyaifar, "Structure and magnetic properties of Zr–Mn-substituted strontium hexaferrite $Sr(Zr,Mn)_xFe_{12-2x}O_{19}$ nanoparticles synthesized by sol–gel auto-combustion method," *Bull. Mater. Sci.*, vol. 39, no. 5, pp. 1311–1318, Sep. 2016, doi: 10.1007/s12034-016-1262-3.

[13] M. J. Iqbal, M. N. Ashiq, P. Hernández-Gómez, J. M. M. Muñoz, and C. T. Cabrera, "Influence of annealing temperature and doping rate on the magnetic properties of Zr–Mn-substituted Sr-hexaferrite nanoparticles," *J. Alloys Compd.*, vol. 500, no. 1, pp. 113–116, Jun. 2010, doi: 10.1016/j.jallcom.2010.03.228.

[14] Z. H. Hua *et al.*, "The effect of La–Zn substitution on the microstructure and magnetic properties of barium ferrites," *Mater. Sci. Eng. A*, vol. 448, no. 1–2, pp. 326–329, Mar. 2007, doi: 10.1016/j.msea.2006.11.153.

[15] A. Ghasemi, "Magnetic properties of substituted strontium ferrite nanoparticles and thin films," *J. Magn. Magn. Mater.*, vol. 324, no. 7, pp. 1375–1380, Apr. 2012, doi: 10.1016/j.jmmm.2011.11.044.

[16] Y. Yang, J. Shao, F. Wang, X. Liu, and D. Huang, "Impacts of Mn–Zn doping on the structural and magnetic properties of M-type Sr–Ca–La hexaferrites," *Appl. Phys. A*, vol. 123, no. 5, p. 309, May 2017, doi: 10.1007/s00339-017-0950-1.

[17] W. Li, X. Qiao, M. Li, T. Liu, and H. X. Peng, "La- and Co substituted M-type barium ferrites processed by sol gel combustion synthesis," *Mater. Res. Bull.*, vol. 48, no. 11, pp. 4449–4453, Nov. 2013, doi: 10.1016/j.materresbull.2013.07.044.

[18] A. Xia, D. Du, P. Li, and Y. Sun, "Crystalline structures and intrinsic magnetic properties of Zn–Ti-substituted hexagonal M-type Ba ferrite powder," *J. Mater. Sci. Mater. Electron.*, vol. 22, no. 3, pp. 223–227, Mar. 2011, doi: 10.1007/s10854-010-0117-8.

[19] L. Peng, L. Li, X. Zhong, Y. Hu, X. Tu, and R. Wang, "Magnetic, electrical, and dielectric properties of La–Cu-substituted Sr-hexaferrites for microwave LTCC devices," *J. Alloys Compd.*, vol. 665, pp. 31–36, Apr. 2016, doi: 10.1016/j.jallcom.2015.12.081.

[20] S. K. Chawla, S. S. Meena, P. Kaur, R. K. Mudsainiyan, and S. M. Yusuf, "Effect of site preferences on structural and magnetic switching properties of Co–Zr-doped strontium hexaferrite $SrCo_xZr_xFe_{12-2x}O_{19}$," *J. Magn. Magn. Mater.*, vol. 378, pp. 84–91, Mar. 2015, doi: 10.1016/j.jmmm.2014.10.168.

[21] V. C. Chavan, S. E. Shirsath, M. L. Mane, R. H. Kadam, and S. S. More, "Transformation of hexagonal to mixed spinel crystal structure and magnetic properties of Co^{2+}-substituted $BaFe_{12}O_{19}$," *J. Magn. Magn. Mater.*, vol. 398, pp. 32–37, Jan. 2016, doi: 10.1016/j.jmmm.2015.09.002.

[22] D. Makovec, D. Primc, S. Šturm, A. Kodre, D. Hanžel, and M. Drofenik, "Structural properties of ultrafine Ba-hexaferrite nanoparticles," *J. Solid State Chem.*, vol. 196, pp. 63–71, Dec. 2012, doi: 10.1016/j.jssc.2012.07.043.

[23] S. B. Galvão, A. C. Lima, S. N. de Medeiros, J. M. Soares, and C. A. Paskocimas, "Effect of morphology on the magnetic properties of barium hexaferrite synthesized by the Pechini method," *Mater. Lett.*, vol. 115, pp. 38–41, Jan. 2014, doi: 10.1016/j.matlet.2013.10.012.

[24] C.-C. Huang *et al.*, "Magnetic property enhancement of cobalt-free M-type strontium hexagonal ferrites by $CaCO_3$ and SiO_2 addition," *Intermetallics*, vol. 89, pp. 111–117, Oct. 2017, doi: 10.1016/j.intermet.2017.06.001.

[25] P. Xu, X. Han, H. Zhao, Z. Liang, and J. Wang, "Effect of stoichiometry on phase formation and magnetic properties of $BaFe_{12}O_{19}$ nanoparticles synthesized by reverse micelle technique," *Mater. Lett.*, vol. 62, no. 8–9, pp. 1305–1308, Mar. 2008, doi: 10.1016/j.matlet.2007.08.039.

[26] B. Hamid, "Effect of magnesium substitution on the structural and magnetic properties of M-type strontium hexaferrite," *Sci. Eng. Appl.*, vol. 2, p. 177, Dec. 2017, doi: 10.26705/SAEA.2017.2.13.177-180.

[27] G. Asghar and M. Anis-ur-Rehman, "Structural, dielectric, and magnetic properties of Cr–Zn-doped strontium hexaferrites for high-frequency applications," *J. Alloys Compd.*, vol. 526, pp. 85–90, Jun. 2012, doi: 10.1016/j.jallcom.2012.02.086.

[28] M. Haseeb, Z. Ali, F. R. Mughal, M. Mushtaq, and N. Algethami, "Tuning magnetic properties of $SrFe_{12}O_{19}$ through La–Co substitution: Site-resolved DFT and experimental insights," *Mater. Today Commun.*, vol. 34, p. 114103, 2025, doi: 10.1016/j.mtcomm.2025.114103.

[29] S. Khademolhoseini and A. Abedini, "A new route for preparation of $SrTiO_3$ nanoparticles with different acids and their photocatalytic application," *J. Mater. Sci. Mater. Electron.*, vol. 28, no. 5, pp. 4403–4408, Mar. 2017, doi: 10.1007/s10854-016-6068-y.

[30] P. Sivakumar, L. Shani, Y. Yeshurun, A. Shaulov, and A. Gedanken, "Facile sonochemical preparation and magnetic properties of strontium hexaferrite ($SrFe_{12}O_{19}$) nanoparticles," *J. Mater. Sci. Mater. Electron.*, vol. 27, pp. 8737–8744, Jun. 2016, doi: 10.1007/s10854-016-4482-9.

[32] M. Haseeb, Z. Ali, F. R. Mughal, M. Mushtaq, and N. Algethami, "Tuning magnetic properties of $SrFe_{12}O_{19}$ through La–Co substitution: Site-resolved DFT and experimental insights," *Materials Today Communications*, vol. 34, Art. no. 114103, 2025, doi: 10.1016/j.mtcomm.2025.114103.

[33] A. Khan, M. Shahzad, and S. Mahmood, "Structural, electronic and magnetic properties of Co-substituted $SrFe_{12}O_{19}$: A DFT study," *Materials Today Communications*, vol. 28, Art. no. 102589, 2021, doi: 10.1016/j.mtcomm.2021.102589.

[34] C. Serletis, G. Litsardakis, E. Pavlidou, and K. G. Efthimiadis, "Magnetic properties of co-precipitated hexaferrite powders with Sm–Co substitutions optimized using the molten flux method," *Phys. B Condens. Matter*, vol. 525, pp. 78–83, Nov. 2017, doi: 10.1016/j.physb.2017.09.025.

[35] M. N. Ashiq, M. Javed Iqbal, and I. H. Gul, "Effect of Al–Cr doping on the structural, magnetic, and dielectric properties of strontium hexaferrite nanomaterials," *J. Magn. Magn. Mater.*, vol. 323, no. 3–4, pp. 259–263, Feb. 2011, doi: 10.1016/j.jmmm.2010.08.054.

[36] M. N. Ashiq, M. Javed Iqbal, and I. H. Gul, "Effect of Al–Cr doping on the structural, magnetic, and dielectric properties of strontium hexaferrite," *J. Magn. Magn. Mater.*, vol. 323, no. 3–4, pp. 259–263, Feb. 2011, doi: 10.1016/j.jmmm.2010.08.054.

[37] "Electronic band structure," *Wikipedia*, 2022. [Online]. Available: https://en.wikipedia.org/wiki/Electronic_band_structure. Accessed: Jan. 2022.

[38] J. R. Christman, *Fundamentals of Solid State Physics*. New York, NY, USA: Wiley, 1988.

[39] R. A. Evarestov and A. V. Bandura, "First-principles calculations on the four phases of $BaTiO_3$," *J. Comput. Chem.*, vol. 33, no. 11, pp. 1123–1130, 2012, doi: 10.1002/jcc.22934.

[40] H.-Y. Zhang, Z.-Y. Zeng, Y.-Q. Zhao, Q. Lu, and Y. Cheng, "First-principles study of lattice dynamics, structural phase transition, and thermodynamic properties of barium titanate," *Z. Naturforsch. A*, vol. 71, pp. 759–767, 2016, doi: 10.1515/zna-2016-0123.

[41] B. Holm, R. Ahuja, Y. Yourdshahyan, B. Johansson, and B. I. Lundqvist, "Elastic and optical properties of α- and κ-Al_2O_3," *Phys. Rev. B*, vol. 59, no. 20, pp. 12777–12787, 1999, doi: 10.1103/PhysRevB.59.12777.

[42] R. Gaillac, P. Pullumbi, and F.-X. Coudert, "ELATE: An open-source online application for analysis and visualization of elastic tensors," *J. Phys. Condens. Matter*, vol. 28, no. 27, p. 275201, 2016, doi: 10.1088/0953-8984/28/27/27.